CONTRIBUTED PAPER

Carrier dynamics and gain saturation in quantum-well lasers

Y. L. LAM

School of Electrical and Electronic Engineering, Nanyang Technological University, Nanyang Avenue, Singapore

J. SINGH

Department of Electrical Engineering and Computer Science, The University of Michigan, Ann Arbor, MI 48109-2122, USA

A Monte Carlo technique has been developed to investigate the carrier dynamics and static gain saturation in graded-index separate confinement heterostructure quantum-well laser structures. The calculated electron relaxation times and gain compression coefficient show good agreement with published experiments.

1. Introduction

In semiconductor lasers, the drive for low threshold current forces one to go towards narrow quantum-well lasers. At the same time, since photons have to be strongly confined in the active region, large-bandgap cladding layers have to be incorporated. As a result, electrons and holes have to be injected into the quantum wells from very high energies and they have to shed $\sim$300 to 500 meV of energy before lasing through the quantum-well state, leading to prolonged carrier capture in both graded-index and ungraded-index separate confinement heterostructure (GRINSCH and SCH, respectively) quantum-well lasers. The carrier relaxation processes, via the nonlinear gain saturation phenomenon, is known to strongly affect the intrinsic modulation speed limit of a semiconductor laser [1–5]. This effect is investigated with the Monte Carlo method in this paper, where both electron relaxation and gain saturation are simultaneously simulated. Using the Monte Carlo approach, unlike the usual density matrix formalisms [1, 6], the details of the electron relaxation process such as intersubband relaxation by polar optical phonon and electron–electron scatterings can be included explicitly. Furthermore, the complications arising from the composition-graded confinement layers can also be handled. Owing to their larger mass and their having less excess energy to shed, the hole relaxation processes are much faster than the electron processes [7–9]. Hence the relaxation processes in the conduction band dominate the device response. For this reason and to simplify the study, the hole effects are not included in this paper.

2. Monte Carlo techniques

The laser structures studied consist of a single $In_{0.2}Ga_{0.8}As$ quantum well (4 to 10 nm width),

sandwiched between symmetrically graded (70% to 14% Al, 200 nm thick) AlGaAs confinement layers. We have developed a Monte Carlo technique to simulate carrier relaxation in these structures. Using this method, we can simulate how an ensemble of carriers injected at the barrier edge progress through the graded-index region, are captured by the quantum well, and relax to their thermal equilibrium.

In our Monte carlo method, we model the carrier transport in the 3D graded-index region and the 2D well region separately. The usual 3D Monte Carlo method [10] is employed to simulate electron transport in the 3D graded-index region; 3D acoustic phonon scattering, polar optical phonon scattering, and inter- and intravalley scattering are considered. The 2D well region includes the quantum-well layer and a thin layer of its neighbouring barrier that experiences significant quantum confinement effects. 2D Monte Carlo simulation is performed in this region. The dominant scattering mechanism in this region is polar optical phonon (POP) scattering. Using the Fermi Golden Rule, the intersubband POP rates are given by [11]

$$S_{mn}^{POP} = \frac{e^2 \omega_0}{8\pi\epsilon_0} \left(\frac{1}{\epsilon_\infty} - \frac{1}{\epsilon_s} \right) (N_q + \tfrac{1}{2} \mp \tfrac{1}{2}) \int \frac{H_{mn}(Q)Q}{Q^2 + Q_0^2} \delta(E(k_2) - E(k_1) \pm \hbar\omega_0) \, dk_2 \qquad (1)$$

where N_q is the phonon occupation number, $\epsilon_\infty = 10.92$ and $\epsilon_s = 12.90$. The initial and final state wavevectors of the electron are k_1 and k_2, while $Q = \pm(k_1 - k_2)$ and q are the phonon wavevector components parallel and perpendicular to the well layer. For simplicity, the carrier screening effects [12] are included in Equation 1 with $Q_0 = (e^2 n/\epsilon_s k_B T)^{1/2}$ as the Debye screening wavevector, where n is the carrier density. The multisubband coupling coefficients are given by

$$H_{mn}(Q) = \int \int dz_1 \, dz_2 F_{mn}(z_1) F_{mn}(z_2) \exp(-Q|z_1 - z_2|) \qquad (2)$$

where $F_{mn}(z) = F_m(z)F_n(z)$. Employing a finite-difference method, we obtain the envelope function $F_m(z)$ by solving the Schrödinger equation that describes the electronic states in the GRINSCH structure. For completeness, we also include the acoustic phonon (ACP) scattering rates in our model, although it is about 100 times smaller than the POP rates.

Electron–electron (e–e) interactions become significant when the carrier density is moderately high. The total screened electron–electron scattering rate for the 3D region is found using the Fermi Golden Rule [13, 14] to be

$$\Gamma_{e-e}(k_0) = \frac{nm^* e^4}{4\pi\hbar^3 \epsilon_0^2 \beta^2 N} \sum_{\text{all } k} \frac{|k_0 - k|}{\beta^2 + |k_0 - k|^2} \qquad (3)$$

where the sum is extended over the N carriers of the 3D ensemble, and $\beta = 0.5Q_0$ is the inverse effective screening length [14]. For the 2D region, the total electron–electron scattering rates are derived by summing over all final states the transition probability of two electrons in subbands i and j scattering into subbands m and n, respectively, after a collision [15]:

$$\Gamma_{im}(k) = \frac{4\pi e^4 m^*}{\hbar^3 A\kappa^2} \sum_{k_0, j, n} f_j(k_0) \int_0^{2\pi} d\theta \frac{|F_{ijmn(q)}|^2}{(q + q_0)^2} \qquad (4)$$

where $q = |g - g'|/2$; g and g' are the relative wavevectors of the initial and final states, respectively. Here, q_0 is the inverse screening length in two dimensions and F_{ijmn} is the form factor giving the strength of this probability. Only dominant scattering processes are considered. They are the pure intrasubband scattering ($i = j = m = n$) and the intrasubband

scattering where $i = m$, $j = n$ and $i \neq j$. We have implemented both the 2D and 3D e–e scattering mechanisms in our model using a rejection method [15, 16].

We have successfully implemented the modelling of the carrier capture and re-emission processes – the 3D ↔ 2D transitions made by the carriers between the 3D and the 2D regions – within the Monte Carlo approach in our model. The technique is based on the reasoning that if we carry out a 2D Monte Carlo calculation for the graded region by including *all* subbands, then in principle the same result can be obtained from a corresponding 3D Monte Carlo calculation. In practice, we find that by considering up to five subbands a satisfactory modelling of the 3D ↔ 2D transitions can be achieved. In our method, we model both the 3D → 2D and 2D → 3D transitions as phonon-assisted processes. A transition energy level E_{tr} is introduced to facilitate the 2D ↔ 3D transition. We carry out the 3D → 2D transition if, upon the termination of a 3D free-flight, the total carrier energy after a phonon emission scattering process is expected to fall below E_{tr}. A final 2D state is chosen from the nearest subband considering energy and momentum conservation. We perform the reverse 2D → 3D transition when the total energy of a well carrier is expected to exceed E_{tr} after a phonon absorption scattering process. To conserve the in-plane energy and momentum, the in-plane wavevector is unchanged. Its z-directed wavevector is then obtained by considering energy conservation; its z-orientation is randomly selected. In our study, we set E_{tr} equal to one $k_B T$ (26 meV) above the subband minimum of the highest (fifth) state being considered. This setting is confirmed with a series of simulation runs. We find essentially no change if E_{tr} is increased somewhat, showing that inclusion of five subband levels is quite adequate.

In addition to the above, the Pauli exclusion principle is invoked during the Monte Carlo simulation, using an array of k-cells and ensuring adherence to the principle in k-space. Details of the Monte Carlo program are presented elsewhere [17, 18].

In Fig. 1 we show a typical carrier relaxation simulation result, the time evolution of the energy distribution of an ensemble of electrons injected from the edge of the confinement layer. The distribution is organized in terms of the total energy (sum of the potential and the
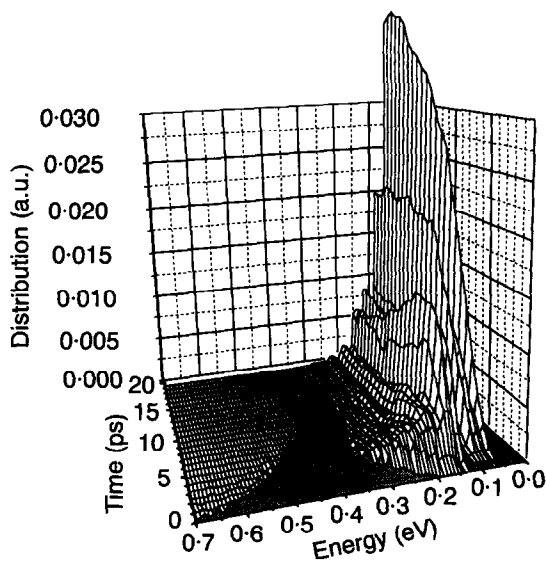

Figure 1 Time evolution of the energy distribution for an ensemble of 10 000 relaxing electrons, injected from the edge of the confinement layer with a kinetic energy of 15 meV at time 0. The simulation is performed on a (linear) L-GRINSCH structure with a 5 nm quantum well, under an applied electric field of 3 kV cm^{-1}. The ensemble of 10 000 electrons is equivalent to an injection density of 10^{16} cm^{-3} in the simulation.
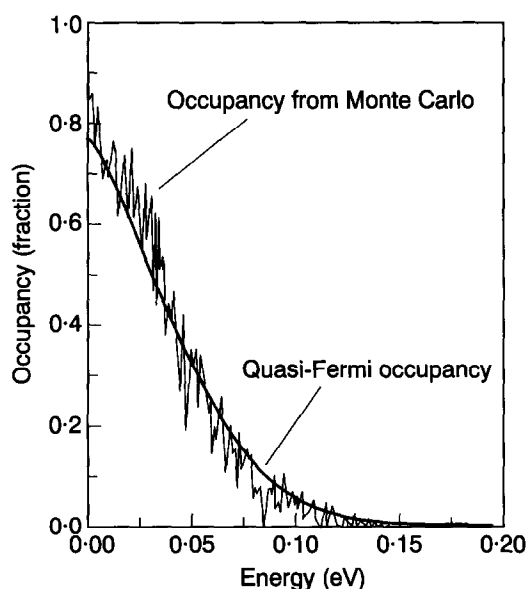
Figure 2 Comparison of the final distribution from the Monte Carlo simulation of Fig. 1, and the analytical quasi-Fermi distribution. The energy distribution of carriers from the simulation is plotted as the occupancy of the well states in this figure.

kinetic energies) of the carrier; the conduction band of the low-bandgap material is the reference energy level. The ensemble of electrons is injected with an initial thermal distribution that is normally distributed with a zero mean in-plane momentum and a non-zero mean velocity-weighted perpendicular plane momentum, corresponding to an injected mean kinetic energy of 15 meV. It is seen in Fig. 1 that after a sufficiently long time (>20 ps), the distribution has reached equilibrium. The final distribution is plotted in Fig. 2 as the occupancy of well states. It is clearly shown in this figure that the final distribution obtained from the simulation compares very well with the analytical quasi-Fermi distribution, as expected.

It is useful to determine the electron capture time and compare it against published experiments. Electron capture is defined in this study as the time taken for the injected carrier to be captured into the ground state (first subband) of the quantum well. The simulation results show that the number of ensemble carriers captured rises roughly as $(1 - \exp(-t/\tau_c))$, where τ_c is the electron capture time constant. In Fig. 3, we show the calculated electron capture time constant obtained from additional simulations for different well widths, and for parabolic graded structures (P-GRINSCH) under similar simulation conditions. The figure shows that carrier relaxations in L-GRINSCH structures are ~30% faster than in P-GRINSCH structures. This result is in good agreement with the experiments of Morin *et al.* [8], where carrier capture time constants of 8.2 ps and 10 ps, compared to our calculated time constants of 6.7 ps and 8.8 ps, are measured for 5 nm well width L-GRINSCH and P-GRINSCH structures, respectively.

In conventional (uncompressed) optical gain spectra calculations [19], the carrier distribution in the active layer is assumed to be in equilibrium and is modelled using quasi-Fermi functions. This is a reasonable assumption if the photon density in the optical cavity is low, when the electron–hole recombination times are ~1 ns while the carrier relaxation time is ~10 ps. However, the quasi-Fermi assumption is not applicable as the stimulated emission rates approach the carrier energy relaxation times under high photon density conditions. In our
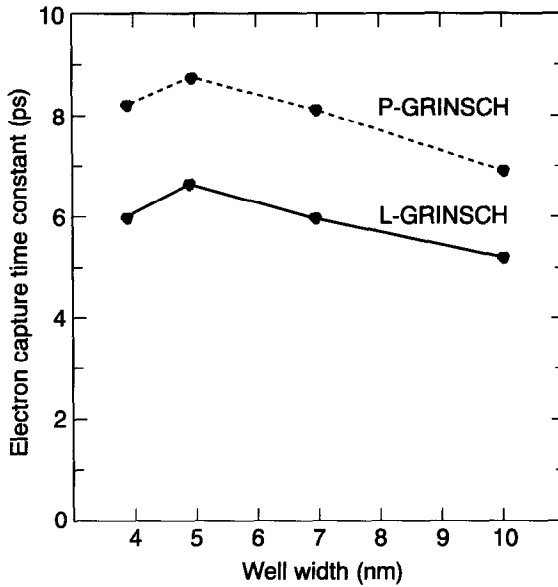
Figure 3 Calculated electron capture time constant as a function of well width for L-GRINSCH and P-GRINSCH (parabolic index grading) 5 nm quantum well structures. The simulation is performed under similar simulation conditions as in Fig. 1.

study, we obtain the carrier distribution from the Monte Carlo simulation of the carrier dynamics, as described above.

Obviously, under intense photon emissions, the carrier dynamics simulation must consider the large amount of accompanying carrier recombination. To do this, the optically coupled region (OCR) of the carrier distribution $f(E)$ is first estimated. We first calculate the optical gain spectra and then obtain the above-threshold steady-state lasing mode solution from the multimode coupled electron–photon rate equations describing the laser operation. This calculation is based on our previous work [20]. From this solution and from consideration of linewidth broadening factors, we then estimate the OCR of the carrier distribution $f(E)$. An additional scattering rate R_{stim} is included for those carriers in the OCR. This rate can be derived from the usual steady-state photon rate equation as

$$R_{stim} = \frac{v_g A \Gamma G S}{N_{ocr}} \tag{5}$$

where v_g is the group velocity, Γ is the optical confinement factor, N_{ocr} is the number of carriers in the OCR, and A is the area considered in the simulation.

3. Gain saturation simulation

A two-step approach is employed to simulate the gain saturation effects in the layer structure to enable direct calculation of the gain compression coefficient. Since gain compression is a material phenomenon, its coefficient is independent of the waveguiding structure, such as whether its facets are antireflection coated. In fact, we find it more convenient to perform our calculations in the latter example of an equivalent travelling-wave optical amplifier. In addition, we make the laser line of the optical input signal coincide with the lasing mode of the would-be laser so that the ensuing simulation applies to the laser situation as well. In the first step, carrier relaxation is simulated to obtain the initial equilibrium state, having a desired

carrier density in the well and a peak optical gain G_1. Since we assume no optical input signal for now, the photon population $S_1 \sim 0$.

Next, we desire a second steady-state solution of the system having a finite photon population S_2. Owing to gain saturation, the associated material gain G_2 will be smaller than G_1. The reduction of the optical gain due to gain compression can be modelled [2] using $G = G_0(1 - \epsilon S)$, where the gain compression coefficient ϵ is given by [21]

$$\epsilon = -\left[\frac{\Delta G}{\Delta S}\frac{1}{G_0}\right]_{S=0} \approx -\frac{G_2 - G_1}{S_2}\frac{1}{G_1} \tag{6}$$

To facilitate the transition from an $S = 0$ initial steady state to the $S \neq 0$ second steady state, a stimulated emission rate of R_{stim} is instantly established by the external CW optical input signal. The photon population S_1 in the active layer is thus given by

$$S_1 = R_{stim}\frac{N_{ocr,1}}{v_g A \Gamma G_1} \tag{7}$$

This stimulated emission rate R_{stim} is held constant throughout the entire Monte Carlo simulation, while the carriers adjust to establish a new steady state, having peak gain G_2, OCR carrier count $N_{ocr,2}$, and a final photon population $S_2 = R_{stim}N_{ocr,2}/v_g A \Gamma G_2$. With these results, the gain compression coefficient can now be calculated using Equation 6. It is noted that holding the stimulated emission rate fixed, or equivalently varying the optical input signal to bring about a change in the photon population from S_1 to S_2, is solely for computational convenience only and does not in any manner affect the compression coefficient calculation, since steady-state analyses are employed here to characterize the gain saturation effects.

Gain saturation is simulated for the L-GRINSCH structure having a 5 nm width quantum well. The initial steady state is established for a carrier density of $\sim 1.1 \times 10^{12}\,cm^{-2}$ in the quantum well, with a Monte Carlo simulation involving an ensemble of 6000 carriers. In equilibrium, most of these carriers (4268 out of 6000) are in the quantum well. The peak gain $G_1 = 640\,cm^{-1}$. To translate the simulation to the second finite S steady state, a stimulated emission rate of $R_{stim} = 10^{10}\,s^{-1}$ (with an OCR of 5 meV FWHM at the band edge) is established. Figure 4 shows the changes in the peak optical gain, the numbers of carriers in the well (N_{well}) and the number of carriers in the optical coupled region (N_{ocr}), respectively, during the transition from the initial zero-photon state to the final finite-photon state.

The gain compression coefficient is calculated with Equation 6 to be $\epsilon = 1.1 \times 10^{-17}\,cm^3$. The magnitudes of ϵ found in published experiments on bulk laser diode are (i) $7 \times 10^{-18}\,cm^3$ to $6.7 \times 10^{-17}\,cm^3$ [2, 22] (from the frequency response); (ii) $10^{-17}\,cm^3$ [23] (from subpicosecond gain dynamics); (iii) $5.4 \times 10^{-18}\,cm^3$ [24] (using a parasitic-free optical modulation technique); and (iv) $1.2 \times 10^{-17}\,cm^3$ [25] (by measuring the intensity modulation spectra of current-modulated Fabry–Perot lasers). The experimental values of ϵ for quantum-well lasers are (i) $\sim 3 \times 10^{-17}\,cm^3$ [26, 27] (from the frequency response); (ii) $4.3 \times 10^{-17}\,cm^3$ [28] (by studying nondegenerate four-wave mixing); and (iii) 2.45 to $7.34 \times 10^{-17}\,cm^3$ [29] (by relative intensity noise measurements). Furthermore, other recent theoretical studies have found the gain compression coefficient to be $1.67 \times 10^{-17}\,cm^3$ [30] and $1.33 \times 10^{-17}\,cm^3$ [31, 32]. Therefore, reasonable agreement has been found
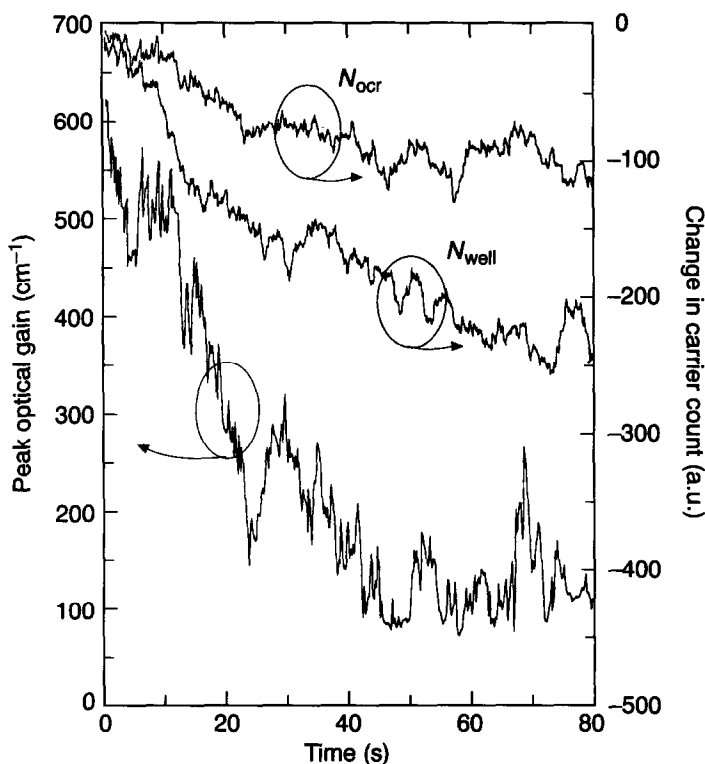
Figure 4 Results of the gain saturation simulation.

between the ϵ values obtained in the present study and published experimental and theoretical studies.

We note that the gain saturation response time is related to the carrier relaxation time, i.e. the time required for a newly injected carrier (replenishing the carriers recombined in stimulated emission) to achieve equilibrium with the carrier population in the well. This is supported by the observation in Fig. 4 that the steady-state N_{well} is lower at higher S, since more carriers are in the transit phase at higher photon emission rates. That is, in a hypothetical situation of faster carrier relaxation, fewer carriers will be in transit and more carriers will be in the well, contributing to the optical gain. We therefore see that the carrier relaxation time is intimately related to the static gain suppression phenomenon — longer relaxation time leads to greater gain compression. We have calculated the threshold carrier density n_{th} for the L-GRINSCH having typical laser parameters [20]; the results are shown in Table I. The electron capture time constants at these threshold densities are also calculated and listed in Table I. It is seen that these times are quite independent of the quantum-well width (within 4 to 10 nm). Hence we expect the gain compression coefficient to be insensitive to variations in the quantum-well width under lasing conditions also.

It is interesting to note from Fig. 4 that the gain saturation response is estimated to have a time constant of about 28 ps. This is clearly longer than the electron capture time constants of 15 to 18 ps given in Table I. This deviation can be explained by noting that the condition under which Fig. 4 has been calculated is for computational convenience only: a fixed stimulated emission rate is used causing the photon population to increase from 3×10^{10} cm^{-2} to eventually $S_2 = 1.7 \times 10^{11}$ cm^{-2}, where it stabilized at gain G_2. The

TABLE I   The 2D and 3D threshold carrier density n_{th} of L-GRINSCH quantum-well lasers and the calculated electron capture time constants at lasing conditions (i.e. at carrier density equal to n_{th})

	Well width (nm)			
	4	5	7	10
2D n_{th} (10^{12} cm^{-2})	1.09	1.10	1.16	1.30
3D n_{th} (10^{18} cm^{-3})	2.74	2.20	1.65	1.30
Electron capture time constant (ps)	15.5	17.8	17.4	18.0

'strict' approach would have required the photon population $S_2 = 1.7 \times 10^{11}$ cm^{-2} to be established immediately and be maintained until the gain stabilized at G_2. We therefore see that Fig. 4 is calculated with a comparatively lower stimulated emission rate at the initial portion of the response simulation. The resulting lower carrier recombination rate (and the corresponding lower carrier reinjection rate) leads to a longer response time, which explains the above observation.

4. Conclusions

We have successfully modelled the carrier relaxation processes and the gain saturation phenomenon in GRINSCH quantum-well lasers, using the Monte Carlo technique. Calculated electron capture times for L-GRINSCH and P-GRINSCH quantum-well laser structures have been found to compare reasonably well with published experiments. From gain saturation simulation, a gain compression coefficient of $\epsilon = 1.1 \times 10^{-17}$ cm^3 is calculated. Furthermore, we have shown that the electron relaxation times are more or less independent of the well width under lasing conditions, implying that the gain saturation effects are also similarly insensitive to the well width variation.

References

1. M. YAMADA and Y. SUEMATSU, *J. Appl. Phys.* **52** (1981) 2653.
2. R. S. TUCKER, *IEEE J. Lightwave Technol.* **3** (1985) 1180.
3. W. RIDEOUT, W. F. SHARFIN, E. S. KOTELES, M. O. VASSEL and B. ELMAN, *IEEE Photon. Technol. Lett.* **3** (1991) 784.
4. S. C. KAN, D. VASSILOVSKI, T. C. WU and K. Y. LAU, *IEEE Photon. Technol. Lett.* **4** (1992) 428.
5. S. C. KAN, D. VASSILOVSKI, T. C. WU and K. Y. LAU, *Appl. Phys. Lett.* **62** (1993) 2307.
6. M. ASADA and Y. SUEMATSU, *IEEE J. Quantum Electron.* **21** (1985) 434.
7. B. DEVEAUD, J. SHAH, T. C. DAMEN and W. T. TSANG, *Appl. Phys. Lett.* **52** (1988) 1886.
8. S. MORIN, B. DEVEAUD, F. CLEROT, K. FUGIWARA and K. MITSUNAGA, *IEEE J. Quantum Electron.* **27** (1991) 1669.
9. R. KERSTING, R. SCHWEDLER, K. WOLTER, K. LEO and H. KURZ, *Phys. Rev. B* **46** (1992) 1639.
10. W. FAWCETT, A. D. BOARDMAN and S. SWAIN, *J. Phys. Chem. Solids* **31** (1970) 1963.
11. K. YOKOYAMA and K. HESS, *Phys. Rev. B* **31** (1985) 6872; K. YOKOYAMA and K. HESS, *Phys. Rev. B* **33** (1986) 5595.
12. B. K. RIDLEY, *Quantum Processes in Semiconductors*, 2nd ed. (Oxford University Press, New York, 1988).
13. C. JACOBONI and P. LUGLI, *The Monte Carlo Method for Semiconductor Device Simulation* (Springer-Verlag, Wien, New York, 1989).
14. P. LUGLI and D. K. FERRY, *Phys. Lett.* **46** (1985) 594.
15. S. M. GOODNICK and P. LUGLI, *Phys. Rev. B* **37** (1988) 2578.
16. R. BRUNETTI, C. JACOBONI, A. MATULIONIS and V. DIENYS, *Physica* **134B** (1985) 369.
17. Y. LAM and J. SINGH, *Appl. Phys. Lett.* **63** (1993) 1874.
18. Y. LAM and J. SINGH, *IEEE J. Quantum Electron.* **30** (1994) 1196 .
19. J P. LOEHR and J. SINGH, *IEEE J. Quantum Electron.* **27** (1991) 708.

20. Y. LAM, J. P. LOEHR and J. SINGH, *IEEE J. Quantum Electron.* **28** (1992) 1248.
21. A. TOMITA, *IEEE Photon. Technol. Lett.* **4** (1992) 342.
22. D. J. CHANNIN, *J. Appl. Phys.* **50** (1979) 3858.
23. M. P. KESLER and E. P. IPPEN, *Appl. Phys. Lett.* **51** (1987) 1765.
24. J. EOM, C. B. SU, J. LACOURSE and R. B. LAUER, *Appl. Phys. Lett.* **56** (1990) 518.
25. R. FRANKENBERGER and R. SCHIMPE, *Appl. Phys. Lett.* **57** (1990) 2520.
26. M. C. TATHAM, C. P. SELTZER, S. D. PERRIN and D. M. COOPER, *Electron. Lett.* **27** (1991) 1278.
27. H LIPSANEN, D. L. COBLENTZ, R. A. LOGAN, R. D. YADVISH, P. A. MORTON and H. TEMKIN, *IEEE Photon. Technol. Lett.* **4** (1992) 673.
28. J. ZHOU, N. PARK, J. W. DAWSON and K. J. VAHALA, *Appl. Phys. Lett.* **62** (1993) 2301.
29. H. YASAKA, K. TAKAHATA and M. NAGANUMA, *IEEE J. Quantum Electron.* **28** (1992) 1294.
30. A. P. DEFONZO and B. GOMATAM, *Appl. Phys. Lett.* **56** (1990) 611.
31. M. WILLATZEN, A. USKOV, J. MØRK, H. OLESEN, B. TROMBORG and A.-P. JAUHO, *IEEE Photon. Technol. Lett.* **3** (1991) 606.
32. M. WILLATZEN, T. TAKAHASHI and Y. ARAKAWA, *IEEE Photon. Technol. Lett.* **4** (1992) 682.